In-situ Additive Manufacturing Deposition Trajectory Monitoring and Compensation with Thermal Camera

Siqi Chen[1], Yuexin Yang[1], Shuai Liu[1], Molong Duan[1,2,*]

[1]Department of Mechanical and Aerospace Engineering,
The Hong Kong University of Science and Technology, Hong Kong SAR, China
[2]HKUST Shenzhen-Hong Kong Collaborative Innovation Research Institute,
Futian, Shenzhen, China

Abstract

Modern additive manufacturing systems still suffer from low fabrication accuracy and speed. This issue is particularly severe for thermal reaction bonding material extrusion systems, where the motion and the deposition processes are coupled. To enhance the deposition accuracy, this work established a method to use real-time in-situ thermal images to capture and compensate for the geometrical accuracy of the printed parts and establish the spatial and temporal relationship between the inaccuracy and the deposition trajectory commands. The paper derives an analytical slender condition to process the printing regions with low curvature while establishing deposition direction allocation methods to account for the trajectory regions with high curvature. Real-time thermal image localization is performed with key printing feature detection and calibration. The localized and calibrated thermal images are aligned with the defined deposition direction to acquire the deposition inaccuracies. With the deposition dynamics considered, the deposition inaccuracy is reduced via dynamic deposition rate compensation. The proposed thermal imaging and compensation techniques have been experimentally verified with a material extrusion experimental platform to illustrate its capabilities to alleviate the deposition inaccuracy during the corner regions.

Keywords: Additive manufacturing, Real-time thermal monitoring, Deposition trajectory compensation.

1. Introduction

Additive manufacturing (AM) is increasingly adopted in aerospace, automotive, and medical applications [1] due to its flexibility and convenience in rapid prototyping [2] and the manufacturability of complex internal structures [3]. Despite its high-speed growth, modern AM still suffers from low precision, low product and process stability, lack of feedback, and insufficient data utilization [4,5]. Among the seven categories of AM [1], material extrusion (MEX) is a representative class widely used [6]. The MEX process is characterized by the strong coupling of the mechanical motion system and the deposition process [7]. The motion coupling leads to MEX having poor accuracy compared to other approaches [6,7] and poses challenges to the AM control systems. For improved printing accuracy, enhanced levels of monitoring and advanced control methods are needed.

Among various monitoring methods (e.g., acoustic, vibration, etc.), thermal monitoring plays a

---

vital role in the AM processes, particularly in the thermal reaction bonding MEX process due to their distinctive heating and cooling cycles. In the MEX process, the filament is heated to the liquid state, deposited from the nozzle, and then solidified in the environment [8]. The temperature distribution of deposited material in the MEX process contains real-time printing performance and deposition conditions, which significantly contribute to the possible printing defects (e.g., porosity, swelling) and printing geometrical accuracy. Besides, the thermal monitoring system has additional benefits due to its non-contact nature and rich spatial/temporal information. To exploit the information, various printing quality monitoring approaches for AM processes have been proposed. Tlegenov et al. [9] established a dynamic model for minimizing nozzle clogging by monitoring nozzle temperature. Zhang et al. [10] used the in-situ monitored surface temperature of the printing part to forecast the geometry in vat photopolymerization. Khanzadeh et al. [11,12] applied thermal monitoring to the melting pool for the prediction of internal structure anomalies (e.g., porosity and mini-cracks). Farshidianfar et al. [13] related real-time cooling rate and melt pool temperature with the microstructure change of the printed part. Thermal images of the printed layer were also used to analyze the thermal phase-changing process in bioprinting [14]. Caltanissetta et al. [15] presented an approach to detect temperature inhomogeneities in the printing part via thermal video imaging. Mazzarisi et al. [16] analyzed the relationship between the thermal gradient with the produced part's metallographic and microhardness. In addition, artificial intelligence (AI) algorithms are also widely used in thermal image processing. Li et al. [17] introduced a deep convolutional neural network model for feature extraction of thermal images. Li et al. [18] proposed a surface roughness prediction model with machine learning according to extruder temperature and some other printing parameters. Tian et al. [19] combined real-time captured thermal images with deep learning for in-situ porosity detection. However, the existing efforts have rarely tried to extract the deposited trajectory time-domain information from the thermal images, particularly in the MEX process, where a relatively long time-varying temperature history is readily available.

With the information from the monitoring system, the dynamic control of the deposition process and motion are key to the printing process [20]. The thermal image's benefit of its rich dynamic, spatial, and temporal information makes it a desirable candidate for control system feedback [21]. Wang et al. [22,23] utilized thermal imaging to build a regression model for surface temperature prediction and real-time layer printing time control. Li et al. [24] applied thermal monitoring to deposited filament for printing speed and temperature control. Salehi and Brandt [25] used a proportional, integral, and derivative (PID) controller to adjust the printer's laser power according to the temperature of the melting pool. Farshidianfar et al. [26] provided a closed-loop controller to manipulate the microstructure based on in-situ thermal images in the powder bed fusion process. However, most existing control methods exploiting the thermal images only adjust the printing parameters; they lack the capability to control the dynamic features during the deposition. These dynamic features are typically from the high-frequency portions of the motion and deposition (e.g., corners, vibration), whose deposition inaccuracy is commonly seen in MEX with motion/deposition coupling.

To close these gaps of dynamic feature monitoring and control in AM processes, this paper builds a real-time thermal monitoring and feedback control system to optimize the deposition trajectory, particularly for the deposition inaccuracy in the corner region. In particular, the proposed

methodology provides the following main contributions:

- An analytical model of the dynamic relationship between deposition/motion trajectory and the printed path geometry of straight-line and corners is established;
- An in-situ thermal images automatic alignment strategy and its connection to the deposition trajectory time-domain signals are established;
- A method to generate deposition compensation trajectory accounting for both deposition inaccuracy and deposition dynamics is established.

The remainder of the paper is structured as follows: Section 2 proposes a model of the printed width calculation of straight-line and corners in MEX and discusses the method for actual deposition width extraction from thermal images. The error between the ideal and actual width is calculated and utilized as the feedback signal for generating the corresponding compensation trajectory. Section 3 shows the experiment details on hardware and software, so with the experiment processing. The comparison of 2D and 3D printed parts with a series of corners before and after compensation is illustrated, and the improvement of deposition inaccuracy is evaluated, followed by the conclusions in Section 4.

2. In-situ monitoring and deposition inaccuracy compensation method

2.1. Printed path geometry modeling and critical slender deposition condition

Considering the MEX process with a moving print head, assume the print head is moving along a given trajectory $x(t)$, $y(t)$ in a single layer with a deposition material flow rate $E(t)$. The printed layer height is assumed to be determined by the layer-to-layer distance, defined as h. The print head velocity $v(t)$ and the unit vector $e(t)$ representing the time-varying printing direction are defined as

$$v(t) = \left[\dot{x}(t),\ \dot{y}(t)\right]^{\top},$$

$$e(t) = \frac{v(t)}{|v(t)|}. \tag{1}$$

The printing direction $e(t)$ is constant when the trajectory is traveling straight, and is time-varying for curved printing paths. With these variables, the exact boundary (including the left and right boundary $x_l(t)$, $y_l(t)$ and $x_r(t)$, $y_r(t)$) of the printed path for an arbitrary curve can be established based on the simple law of mass conservation. To enable the later dynamic manipulation of the deposition process, a general time-varying flow rate $E(t)$ is assumed.

For the deposition along a straight line, the total deposited material Q from time t_0 to t_1 is given by

$$Q = \int_{t_0}^{t_1} E(t)\,dt = 2h \int_{t_0}^{t_1} |v(t)|\,w(t)\,dt, \tag{2}$$

where w is the half-width of the printed path. It is also assumed that steady-state initial and ending flow rates are E_0 and E_1, respectively. Since Eq. (2) needs to be satisfied for all t, the printed path half-width

w, without considering deposition delay and printed height variation, is thus derived as

$$w(t) = \frac{E(t)}{2h|v(t)|}. \tag{3}$$

Note that the printed path half-width is constant when the flow rate and the printing velocity are constant for the deposition along the straight line.
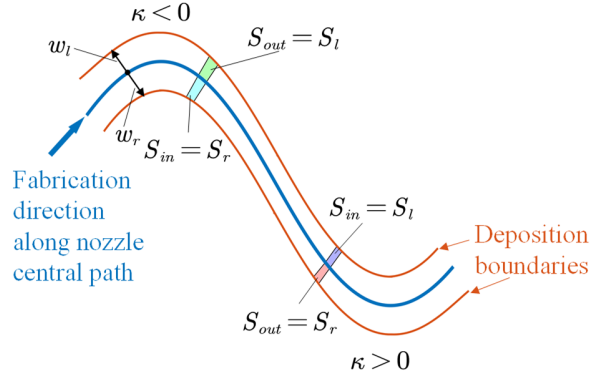

Figure 1 Width calculation illustration for slender deposition path

For more complex cases when the printed materials are deposited along a curved path, similar constitutive law can be derived from the curvature $\kappa(t)$ given by

$$\kappa = \frac{x'y'' - x''y'}{(x'^2 + y'^2)^{\frac{3}{2}}}, \tag{4}$$

where x', x'', y' and y'' are the first- and second-order curve derivatives of the x and y axis, respectively. Note that the curvature κ is positive for counterclockwise rotation in movement direction and is negative for clockwise movement.

Consider the deposition process at a particular time instant as shown in Figure 1, S_l and S_r as the material deposition area on the left and right of the curve. Assuming the deposition process yields a slender curve (i.e., the major deposited material is perpendicular to the path center line), the incremental deposited area on the left and the right of the curve center line along a small curve length ds is calculated as

$$S_l(t) = w_l ds - \frac{1}{2}w_l^2 d\alpha = w_l\left(1 - \frac{w_l}{2}\kappa\right)ds, \tag{5}$$

$$S_r(t) = w_r ds + \frac{1}{2}w_r^2 d\alpha = w_r\left(1 + \frac{w_r}{2}\kappa\right)ds, \tag{6}$$

where $d\alpha$ is the incremental change of the printing direction (positive value indicates counterclockwise

4

rotation, same as the sign of curvature κ). It is assumed that, along the printing direction $e(t)$, the material deposited on one side of the trajectory remains on that side, i.e.,

$$S_l = S_r = \frac{E}{2|v|h}ds.$$ (7)

Combining Eqs. (5) to (7), the left and right printed half width satisfies the following equations

$$\frac{\kappa}{2}w_l^2 - w_l + \frac{E}{2|v|h} = 0,$$ (8)

$$\frac{\kappa}{2}w_r^2 + w_r - \frac{E}{2|v|h} = 0.$$ (9)

The solutions to these two equations are

$$w_l(t) = \frac{1 - \sqrt{1 - \frac{\kappa E}{|v|h}}}{\kappa},$$ (10)

$$w_r(t) = \frac{-1 + \sqrt{1 + \frac{\kappa E}{|v|h}}}{\kappa}.$$ (11)

Note that Eqs. (8) and (9) only have real solutions when

$$S_c(t) \triangleq \left| \frac{\kappa(t)E(t)}{|v(t)|h} \right| \leqslant 1.$$ (12)

This condition is defined as slender deposition condition. The slender deposition condition indicates that the deposition process is mainly along the perpendicular direction of the center line, such that the deposited line is a slender curve. However, this slender deposition condition may not always hold, particularly at corner regions where the curvatures are high. Around these regions, the slender deposition condition is typically violated. This indicates that the printing deposition direction can no longer be interpreted as perpendicular to the printing direction, and additional mathematical treatments are needed to correlate the deposition's spatial and temporal information.

2.2. Deposition direction allocation for high-curvature regions

To alleviate the issues of the high-curvature portions of the trajectory violating the slender deposition condition, a deposition direction allocation method (DDA) method is established to modify the assumed deposition direction, avoiding the possible intersection of the printed path boundaries. At normal regions of the trajectory where the curvature is small (satisfying slender deposition condition in Eq. (12)), the

deposition direction is perpendicular to the printing direction. When curvature is large, an additional rotation angle $\phi(t)$ is introduced. The equivalent added curvature $\kappa_\phi(t)$ is defined as

$$\kappa_\phi(t) = \frac{d\phi}{ds} = \frac{d\phi}{dt}\frac{1}{v(t)}. \tag{13}$$

This rotation angle grants additional freedom to minimize the curvature for the slender deposition condition. Define the effective curvature as

$$\kappa_{eff}(t) = \kappa(t) + \kappa_\phi(t). \tag{14}$$

The slender deposition condition in Eq. (12) is modified to

$$S_c(t) \triangleq \left| \frac{\kappa_{eff}(t) E(t)}{|v(t)|h} \right| \leqslant 1. \tag{15}$$

On the other hand, the design of κ_ϕ in DDA is not completely free. It is expected to minimally change the normal regions that abide by the slender deposition condition. Define s_0 and s_1 are the representative curve length sufficiently far from the regions that need added curvature, while t_0 and t_1 are their corresponding time. The deposition direction orientation with and without DDA should be the same, i.e., the following spatial and temporal relationships should be satisfied:

$$\begin{aligned}
\int_{s_0}^{s_1} \kappa(s)\,ds &= \int_{s_0}^{s_1} (\kappa(s) + \kappa_\phi(s))\,ds, \\
\int_{t_0}^{t_1} \kappa(t)v(t)\,dt &= \int_{t_0}^{t_1} (\kappa(t) + \kappa_\phi(t))v(t)\,dt.
\end{aligned} \tag{16}$$

This condition can be achieved by the allocation of the high κ regions to its neighborhoods, as long as the high curvature regions are only consisting of a small portion within the entire trajectory. This is the fundamental concepts introduced by DDA.

The detailed iterative DDA implementation process is shown in Figure 2. Zero additional curvature (i.e., $\kappa_\phi = 0$) is firstly assumed, while $S_c(t)$ along the entire trajectory is evaluated. The timespan where $S_c(t)$ continuously exhibiting larger than one absolute value is extracted. Define the first continuous timespan that violates Eq. (15) to be $\boldsymbol{t}_v$, which start from $t_{v,0}$ and ends at $t_{v,1}$. The corresponding $\kappa_\phi(t)$ values when $t \in \boldsymbol{t}_v$ are designed to enforce effective curvature $\kappa_{eff}(t)$ to satisfy Eq. (15). i.e.,

$$\kappa_\phi(t) = \begin{cases} \dfrac{|v(t)|h}{E(t)} - \kappa(t) & (\text{when } \kappa_{eff} > 0) \\[2ex] -\dfrac{|v(t)|h}{E(t)} - \kappa(t) & (\text{when } \kappa_{eff} < 0) \end{cases}. \tag{17}$$

The rotation angle error due to the introduction of $\kappa_\phi(t)$ is defined as $\Delta\Phi$ given by

$$\Delta\Phi = \int_{t \in \mathbf{t}_v} \kappa_\phi(t) v(t) dt. \tag{18}$$

This additional rotation angle is designed to be redistributed to the neighborhood of $\mathbf{t}_v$. To maintain the symmetry of the path, the value $\Delta\Phi$ is equally split to the past and future timespan, satisfying

$$\Delta\Phi_f = \Delta\Phi_p = \frac{1}{2}\Delta\Phi, \tag{19}$$

where $\Delta\Phi_f$ and $\Delta\Phi_p$ are the rotation angle introduced in the future and past timespan.

The allocations of $\Delta\Phi_f$ and $\Delta\Phi_p$ are performed in a discrete system with sampling time T_s, representations with defined future and past timespan to be $\mathbf{t}_f = \{t_{f,1}, t_{f,2}, \cdots, t_{f,N_f}\}$, and $\mathbf{t}_p = \{t_{p,N_p}, t_{p,N_p-1}, \cdots, t_{p,1}\}$, respectively. The element in $\mathbf{t}_f$ and $\mathbf{t}_p$ is defined as

$$\begin{aligned} t_{f,j} &= t_{v,1} + jT_s, \\ t_{p,j} &= t_{v,0} - jT_s. \end{aligned} \tag{20}$$

Define $\phi_f(t_{f,j})$ as the remaining rotation angle left for reallocation from $t_{f,j}$. From $t_{f,1}$ to t_{f,N_f}, this sequence of $\phi_f(t_{f,j})$ is strictly monotonically increasing or decreasing to reach zero at t_{f,N_f}; the direction depends on the sign of the initial condition $\phi_f(t_{f,1})$. This procedure is enforced by the relationship

$$\phi_f(t_{f,j+1}) = \phi_f(t_{f,j}) - d\phi_f(t_{f,j}), \tag{21}$$

where $\phi_f(t_{f,j})$ is the additional rotation angle caused by curvature reallocation at $t_{f,j}$ and is kept to be positive or negative for the entire $\mathbf{t}_f$. Following the relationship between curvature and rotation angle in Eq. (13), $d\phi_f(t_{f,j})$ is calculated as

$$d\phi_f(t_{f,j}) = (\kappa(t_{f,j}) + \kappa_\phi(t_{f,j})) v(t_{f,j}) T_s, \tag{22}$$

where $\kappa_\phi(t_{f,j})$ is the additional curvature caused by rotation angle reallocation at $t_{f,j}$. To determine the

additional curvature $\kappa_\phi(t_{f,j})$, the method first calculates the maximum allowance of additional curvature $\hat{\kappa}_m(t_{f,j})$ at $t_{f,j}$ satisfying the slender condition, given by

$$\hat{\kappa}_m(t_{f,j}) = \begin{cases} \dfrac{|v(t_{f,j})|h}{E(t_{f,j})} - \kappa(t_{f,j}) & (\text{when } S_c(t_{f,j}) > 0) \\ -\dfrac{|v(t_{f,j})|h}{E(t_{f,j})} - \kappa(t_{f,j}) & (\text{when } S_c(t_{f,j}) < 0) \end{cases}. \tag{23}$$

The corresponding curvature $\hat{\kappa}_\phi(t_{f,j})$ candidate at $t_{f,j}$ is given by

$$\hat{\kappa}_\phi(t_{f,j}) = \frac{\phi_f(t_{f,j})}{T_s} \frac{1}{v(t_{f,j})}. \tag{24}$$

The candidate is then verified if it satisfies the maximum allowance defined in Eq. (23) (i.e., $|\hat{\kappa}_\phi(t_{f,j})| < |\hat{\kappa}_m(t_{f,j})|$.). This verification further defines the actual $t_{f,j}$ applied in the curvature reallocation procedure with the following formula

$$\kappa_\phi(t_{f,j}) = \begin{cases} \hat{\kappa}_m(t_{f,j}) & (\text{when } |\hat{\kappa}_\phi(t_{f,j})| > |\hat{\kappa}_m(t_{f,j})|) \\ \hat{\kappa}_\phi(t_{f,j}) & (\text{when } |\hat{\kappa}_\phi(t_{f,j})| \leq |\hat{\kappa}_m(t_{f,j})|) \end{cases}. \tag{25}$$

With $t_{f,j}$ calculated, the corresponding effective rotation angle at $t_{f,j}$ is calculated as

$$\phi_{eff}(t_{f,j}) = \kappa_{eff}(t_{f,j})v(t_{f,j})T_s. \tag{26}$$

Now the additional rotation angle $d\phi_f(t_{f,j})$ allocated at $t_{f,j}$ and the residual additional rotation angle awaiting reallocation $\phi_f(t_{f,j+1})$ at the next time $t_{f,j+1}$ are calculated, following Eqs. (21) and (22). The operation is repeated until $\phi_f(t_{f,j+1}) = 0$ indicating that the reallocation of $\Delta\Phi_f$ in $\boldsymbol{t}_f$ is finished. This also defines the discrete steps needed for the reallocation process N_f.

The same reallocation method is operated for $\Delta\Phi_p$ in $\boldsymbol{t}_p$ with a similar process in the backward direction. When finishing reallocation in both $\boldsymbol{t}_f$ and $\boldsymbol{t}_p$, the slender condition violation at $\boldsymbol{t}_v$ has been fully addressed. Note that this reallocation process only addresses one continuous timespan that violates the slender condition; there typically still exists multiple similar continuous timespans, which can be recursively addressed by redefining $\boldsymbol{t}_v$ to the next violation. This recursive handling is repeated until $\boldsymbol{t}_v = \varnothing$, indicating the curvature smoothing process is finished. This complete DDA process establishes the local deposition direction for arbitrary continuous trajectory. The results with and without the DDA process are illustrated in Figure 3. It can be seen that the estimated boundary expands at the cornering

regions with large κ and low velocities. Also, the primary deposition directions (marked in red) are continuously distributed in the neighborhood of the cornering regions without intersection due to the introduction of κ_{eff}.
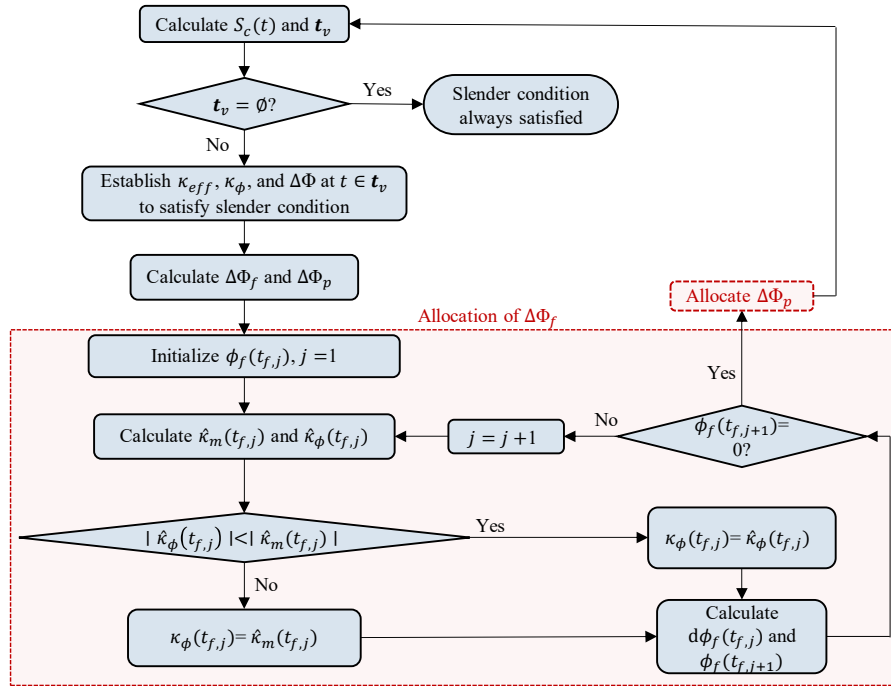

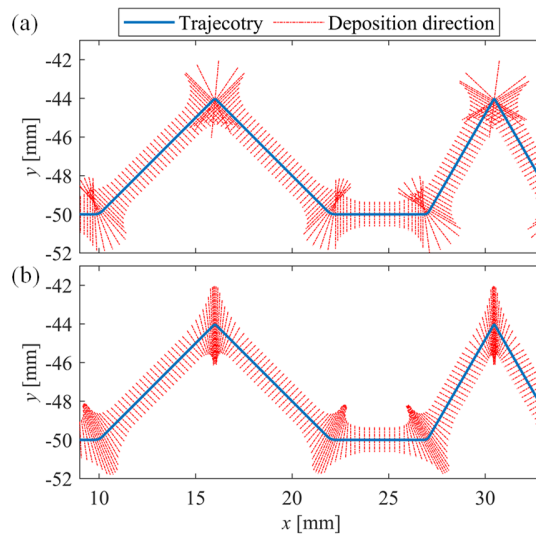Figure 2 Flow chart for deposition direction allocation avoiding slender condition violation

Figure 3 The principal deposition directions (a) without and (b) with deposition direction allocation

9

2.3. *Thermal image processing, stitching, and localization*

With deposition direction defined, the thermal image could align the captured deposited path to its temporal deposition information. This process requires the thermal image calibration, stitching, and localization. Note that the thermal images typically have blurry boundaries (compared to conventional optimal images) due to the heat flux. This causes additional challenges for its calibration. The thermal image distortion, similar to conventional optimal images, is decomposed to radial distortion and distortion due to tilted camera alignment. The radial distortion is the camera's intrinsic parameter; it is conventionally addressed by applying Zhang's method [27], where the radial coefficients are identified with chessboard calibration images. The distortion due to tilted camera alignment is typically inevitable in AM monitoring process since the camera can only monitor the heat-affected regions from the side. This distortion can be addressed by homography transformation. Define a 2D generalized vector in the image coordinate frame and the ground coordinate frame to be $P^{(0)} = \{a^{(0)}, \ b^{(0)}, \ 1\}^{\top}$ and $P^{(1)} = \{a^{(1)}, \ b^{(1)}, \ 1\}^{\top}$ and a homography matrix H satisfying

$$P^{(1)} = HP^{(0)} = \begin{bmatrix} h_{11} & h_{12} & h_{13} \\ h_{21} & h_{22} & h_{23} \\ h_{31} & h_{32} & h_{33} \end{bmatrix} P^{(0)}. \tag{27}$$

Since the homography matrix H has 8 degrees of freedom [28], at least four pairs of corresponding points are required to get its solution. As the MEX method contains plenty of dynamic features, the corner points' position in thermal images and their corresponding corners in geometric printing trajectory are selected as the pairs for H matrix calculation. Note that as the thermal camera, which is attached to the nozzle is moving during the whole printing process, the H matrix is a function of time. For each thermal image, the H matrix might need to be recalculated, which is caused by the change of image capture conditions like the tilt angle of the thermal camera.

The conventional corner detection techniques, such as Haris, rely on significant gradient fluctuations in the image [29], which are unsuitable for thermal images with blurring edges due to heat flux. As the accumulation of heat at printing corners (usually caused by over-deposition in corners), feature extraction provides another way for corner point detection in thermal images. The feature extraction in thermal images in this work adopts the fast region-based convolutional neural networks (Fast R-CNN) model presented by Ren et al. [30] (with ResNet-50 as the backbone) while combining the Feature Pyramid Network (FPN) presented by Lin et al. [31] to enhance the feature detection robustness. The resultant detected feature boxes provide the thermal image corner estimations. Considering that the feature close to the edge of the image may be incomplete, those points whose distance to the image edge is less than 5% of the image size are removed. These detected corners are used to calibrate the thermal images as well as localize the thermal images with printed trajectory. The detected corners in the thermal image formulate the set of $P^{(0)}$ while the set of known physical points formulates the set of $P^{(1)}$, as Eq. (27) indicates. The homography transformation matrix H is thus calculated with least square algorithms. Solving H matrix requires at least four corners in an image to provide enough information. Figure 4 (b) shows the corner detection result of the first aligned thermal image after cropping to the rich information area, and Figure 4 (c) shows the localization result of the first aligned image.
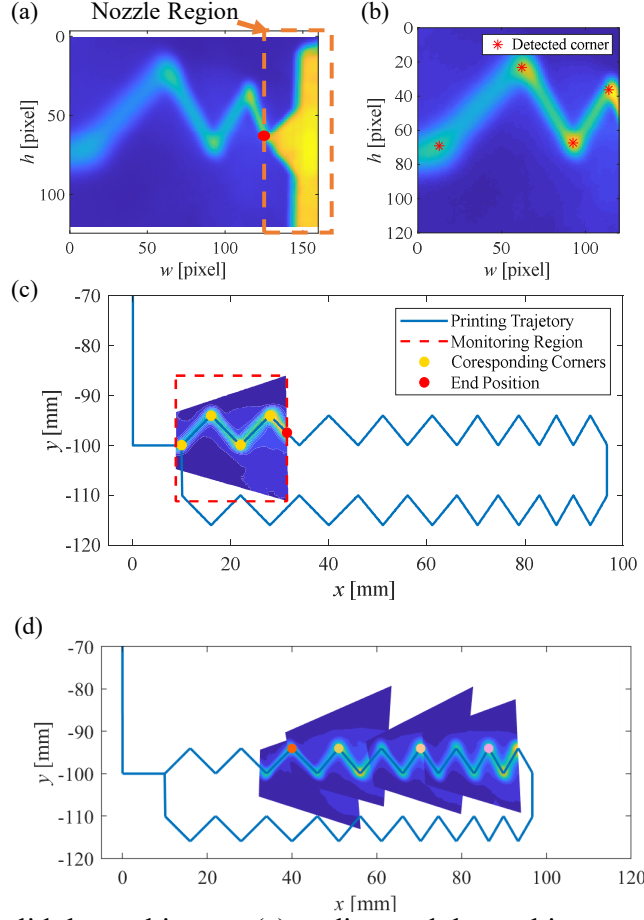
Figure 4 Alignment of valid thermal image: (a) undistorted thermal image, (b) rich-information thermal image with the detected corner, (c) aligned result of the first thermal image, and (d) alignment of in-situ thermal images

Although the thermal camera is commanded to acquire the thermal image at a fixed rate, the actual image capture time instant has slight fluctuations and thus needs localization. The key to localization is the knowledge of the thermal image capture time instant. Define the ith thermal image's true capture time, recorded time, and unknown time fluctuations to be $t_c(i)$, $t_r(i)$, $t_f(i)$, satisfying

$$t_c(i) = t_r(i) + t_f(i). \tag{28}$$

The fluctuations $t_f(0)$ is relatively small and thus $t_r(0)$ is typically used to estimate $t_c(0)$. Since the geometrical relationship between the thermal camera and printing nozzle is unchanged during the monitoring process, the nozzle position in the image frame is manually marked in the first aligned thermal image and defined as $P_N^{(0)} = \{a_N^{(0)}, b_N^{(0)}, 1\}^\top$. The nozzle position and the monitoring region of the ith thermal image of the ground frame are defined as $P_{N,i}^{(1)} = \{a_{N,i}^{(1)}, b_{N,i}^{(1)}, 1\}^\top$ and $\boldsymbol{R}_i^{(1)}$, respectively. The recorded time $t_r(i)$ gives the approximated nozzle position $\hat{P}_{N,i}^{(1)}$ and expected monitoring region $\boldsymbol{R}_i^{(1)}$ of

the ith thermal image. The corners in the ith thermal image and in the trajectory within $\boldsymbol{R}_i^{(1)}$ is detected, and they give the homography matrix $H(i)$ following Eq. (27). The actual nozzle position $P_{N,i}^{(1)}$ in the ground coordinate frame for the ith thermal image is thus given by

$$P_{N,i}^{(1)} = H(i) P_N^{(0)}. \tag{29}$$

The calculated nozzle coordinate $P_{N,i}^{(1)}$, combined with the trajectory $x(t)$ and $y(t)$ in Eq. (1), is used to provide the estimation of the capture time instant, given by

$$\hat{t}_c(i) = \operatorname*{argmin}_{t \in U(t_r(i), \delta t)} \left\{ \| (x(t), y(t)) - (a_{N,i}^{(1)}, b_{N,i}^{(1)}) \|^2 \right\}. \tag{30}$$

where $U(t_r(i), \delta t)$ is the neighborhood of $t_r(i)$ with a small timespan δt. For typical thermal images, δt should be within 10 ms. Now capture time instant $t_c(i)$ of the ith thermal image is accurately known, indicating that the localization of the thermal image is precisely aligned with the ground frame. Compared with the two-step calibration and localization method that calculates the calibration matrix and then does the alignment [32], the proposed method calibrates and localizes the thermal image with the trajectory simultaneously, which increases the computation efficiency and automation. The proposed method also eliminates the error of thermal image calibration caused by the image capture condition changing during printing (e.g., vibration, tilt angle change) as the H matrix is recalculated under a specific image capture condition. The resultant in-situ thermal images are shown in Figure 4 (d).

2.4. Deposition information extraction and dynamic deposition compensation method

With the DDA process and thermal image processing, the thermal-image-enabled dynamic deposition trajectory compensation (T-DDTC) method is established in this section. The deposition information at each sampling time at the trajectory $x(t)$, $y(t)$ is extracted along the critical deposition direction derived in Section 2.2 for each localized thermal image, as shown in Figure 5 (a). The contour with the threshold temperature T_t is applied to extract the left and right deposition half-width $w_l(T_t, t)$ and $w_r(T_t, t)$. Define the desirable printed path half-width to be $w_d(t)$ given by

$$w_d(t) = \frac{w_0}{\cos(\phi_{eff}(t))}, \tag{31}$$

where $\phi_{eff}(t)$ is the effective rotation angle defined in Eq. (26) and w_0 is the theoretical width of a straight printed path. Correspondingly, the error of deposition width Δw is defined as

$$\Delta w = w_l(T_t, t) + w_r(T_t, t) - 2w_d(t), \tag{32}$$

Define ϵ as the maximum tolerable deposition inaccuracy; deposited regions satisfying $|\Delta w| \geqslant \epsilon$

12

indicates significant deposition inaccuracies that require compensation. Define Δt_0 and Δt_1 as starting and ending time of a continuous deposition inaccuracy timespan $\boldsymbol{t}_o$, respectively. The extracted and perfect width in a continuous deposition inaccuracy timespan collected from Figure 5 (a) is shown in Figure 5 (b). According to the deposition inaccuracy Δw, the local deposition compensation rate is estimated to be

$$\Delta E(t) = K_e(w_l + w_r - 2w_d), \tag{33}$$

where K_e is a deposition correction gain.

To achieve desirable compensation results, the dynamic of the deposition process needs to be considered. This arises from the fact that there is typically a delay between the deposition signal and the actual deposition process. Define the deposition compensation reference command to be $\Delta E_t(t)$ and the actual deposition variation is $\Delta E_r(t)$. This input-output is researched by Bellini et al. [33] and Wu et al. [34], and their works adopt a first-order linear time-invariant (LTI) system representation $G(s)$ for its relationship, given by

$$\Delta E(s) = \underbrace{\frac{1}{\tau s + 1}}_{G(s)} \Delta E_r(s), \tag{34}$$

where s is the Laplace variable; τ is the time constant; $\Delta E_r(s)$ and $\Delta E(s)$ are the Laplace transform of $\Delta E_r(t)$ and $\Delta E(t)$. Its time-domain representation is written as

$$\Delta E_r(t) = \Delta E(t) + \tau \frac{d\Delta E}{dt}. \tag{35}$$

Considering the dynamic of deposition, the compensation timespan is extended to $\hat{\boldsymbol{t}}_o$, with starting and ending time at $\Delta \hat{t}_0$ and $\Delta \hat{t}_1$. The corresponding input deposition compensation velocity trajectory $v_{er}(\Delta t)$ is smoothened with an m order non-uniform rational basis spline (NURBS) as

$$\Delta \hat{v}_{er}(\Delta t) = \sum_{i=0}^{n} N_i(\Delta t) P_i, \tag{36}$$

where $\Delta t \in \left[\Delta \hat{t}_0, \Delta \hat{t}_1\right]$; $N_i(\Delta t)$ is the basis function; $P_i = \{\Delta t_i, \Delta V_i\}^\top$ is the control point defining the pairs of compensation velocity at a particular time. To guarantee a smooth transition with the uncompensated regions, the final input deposition velocity $v_{ef}(\Delta t)$ satisfies

$$v_{ef}(\Delta t) = v_e(\Delta t) - \Delta v_{er}(\Delta t), \tag{37}$$

13

where $v_e(\Delta t)$ is the original input deposition velocity.
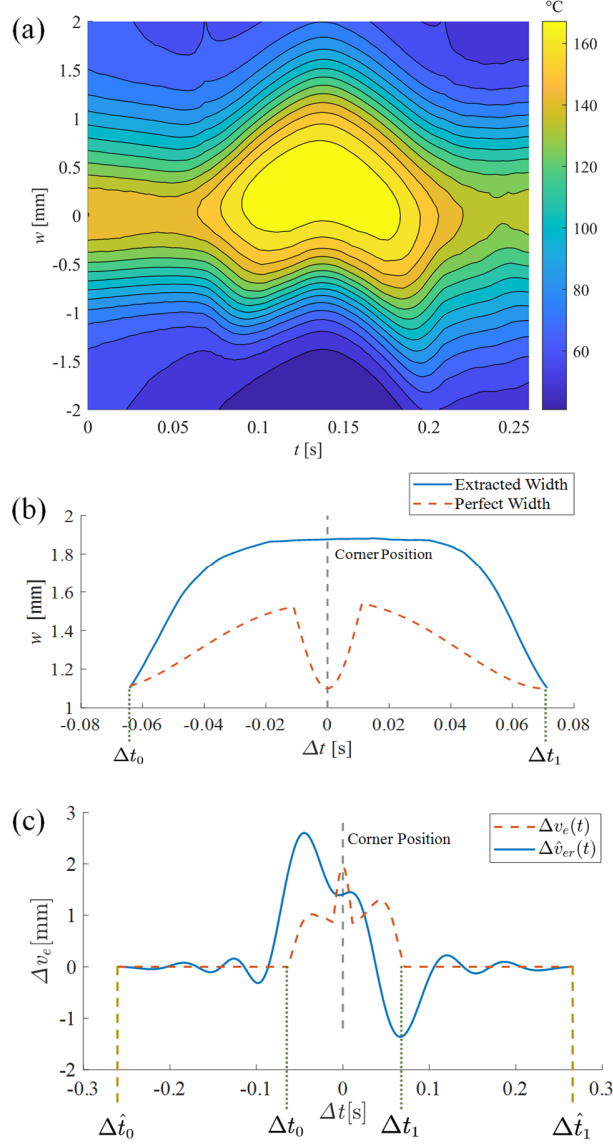

Figure 5 Compensation trajectory generation process: (a) temperature distribution converted to the deposition direction and time, (b) extracted printed width and desirable printed width in a continuous timespan, and (c) deposition compensation sequence

According to the filtered B-spline (FBS) approach proposed by Duan et al. [35], the transfer function $G(s)$ in Eq. (34) is applied to $N_i(\Delta t)$ to obtain the filter basis function $\widetilde{N}_i(\Delta t)$. Accordingly, the desired output deposition compensation velocity $\hat{v}_e(\Delta t)$ is calculated as

$$\Delta \hat{v}_e \left(\Delta t \right) = \sum_{i=0}^{n} \widetilde{N}_i \left(\Delta t \right) P_i. \tag{38}$$

The control points $P_i = \{ \Delta t_i, \Delta V_i \}^{\top}$ are obtained by the minimum optimization with

$$\begin{aligned}
P_i &= \operatorname{argmin} \left\{ \| \Delta \hat{v}_e \left(\Delta t \right) - \Delta v_e \left(\Delta t \right) \|^2 \right\}, \\
\text{s.t. } & \Delta V_{\min} \leqslant \Delta V_i \leqslant \Delta V_{\max}, \\
& P_0 = \left(\Delta \hat{t}_0, 0 \right), \\
& P_n = \left(\Delta \hat{t}_1, 0 \right).
\end{aligned} \tag{39}$$

The range of ΔV_i is constrained considering origin deposition velocity and deposition dynamics with the minimum and maximum compensation velocity. Figure 5 (c) shows the calculated result of the desired input $\Delta \hat{v}_{er} \left(\Delta t \right)$ and perfect output $\Delta v_e \left(\Delta t \right)$ of deposition compensation velocity. Note that the generated deposition compensation sequences could be restored as a database and reused in further printing for similar trajectories. The application of the database saves needs of computation resources of the T-DDTC system. However, under different printing conditions (like the change of viscosity and fluidity of printing materials, nozzle health conditions, the flatness of the base plate, or the previous layer), the deposition inaccuracy circumstance might deviate from the previously collected one. Therefore, if higher geometry accuracy is needed for the printing part, the real-time thermal monitoring and compensation system should be applied to the whole printing process.

3. Experiment Verification of Proposed Method

3.1. Experimental hardware setup

Figure 6 shows the setup of the experiment. The Flashforge Creator 3 MEX printer is used for the experiments. The thermal camera (FLIR 3.5) is fixed on a printed lightweight fixture tightly installed on the printing nozzle and moves with the nozzle during printing. The installation of the thermal camera helps in capturing real-time deposition situations. The printing parameters and the camera specifications are specified in Table 1 and Table 2, respectively. Note that the thermal expansion of PLA in the targeted range is minimal: A 200 °C drop in temperature only causes 0.0041% 1D shrinkage. Therefore, the thermal expansion in the thermal image is omitted in this case.

The main testing trajectory includes different angles of corners (as illustrated in Figure 7 (a)) due to MEX process being typically rich in corner features. To further validate the efficiency of enhancing deposition accuracy during the layer-by-layer fabrication, the testing part consisting of 20 layers of the testing trajectory is designed, shown in Figure 7 (b). A baseplate is added to provide a flat and solid base for the main trajectory printing, despite the problem caused by the leveling of the print bed. The 3D printed parts with and without the proposed T-DDTC method are evaluated.

Table 1 Printing parameters

Printer maximum size	$300 \times 250 \times 200$ mm^3
Printer name	Flashforge Creator 3
Nozzle diameter	0.4 mm
Layer height	0.25 mm
Printing speed	20 mm/s
Acceleration	500 mm/s^2
Corner trajectory blending tolerance	0.05 mm
Printing material	PLA
Thermal expansion coefficient	41 μm/(m·K)
Nozzle temperature	230 °C
Print bed temperature	60 °C

Table 2 Thermal camera specifications

Type	FLIR 3.5
Maximum frame rate	9 Hz
Minimum temperature	-10 °C
Maximum temperature	450 °C
Weight	0.9 gram
Resolution	160×120
Thermal sensitivity	<50 mK (0.050° C)
Tilt angle	45°
Distance to the printing plane	14.5 mm
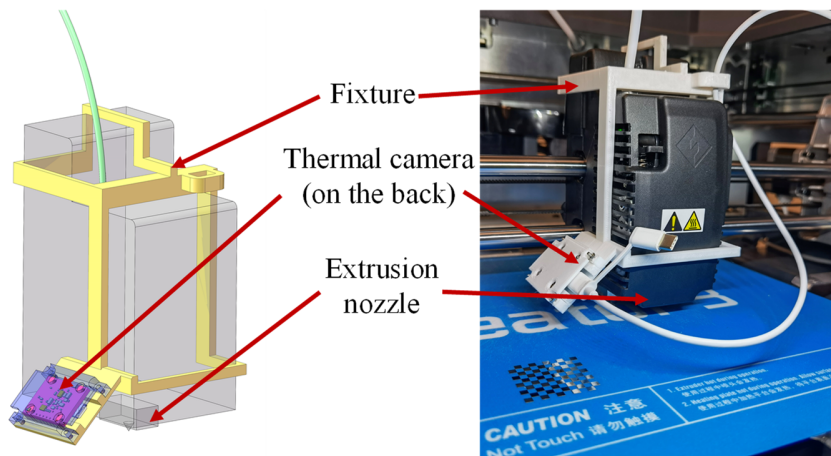
Figure 6 Experimental MEX deposition nozzle with thermal camera [32]

3.2. Thermal image processing and compensation trajectory generation

The first step in thermal image processing is corner detection. The images for corner detection model training are carefully annotated with one class (corner) using the mature and efficient image labeling manner [36]. There are total 69 annotated images with more than 200 features. The image dataset is packaged in the form of PASCAL VOC 2012 [37] and is randomly divided into train and test sets in a 1:1 ratio. The initial learning rate is set to be 0.01. The batch size for training is set to 2, and the epoch size is 15. The mean Average Precision (mAP) value of the model generated from each epoch is calculated according to the evaluation standard. The mAP of the final trained model selected is 99.5%, demonstrating high accuracy and precision. The monitoring system starts to capture and process thermal images after the beginning of main trajectory printing. The thermal images are first marked with the nozzle position and cropped, with the information-rich region remaining. With the pre-trained detection model, real-time captured images are sent for corner feature detection. The time interval of each thermal image is set to 0.125 s. The hardware of thermal image processing is an i5-12500H CPU and a single NVIDIA GeForce RTX 2050 GPU.
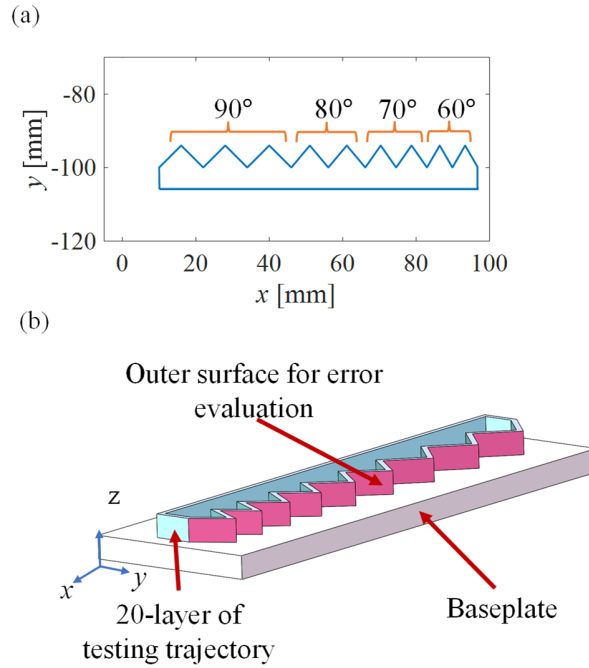

Figure 7 (a) A 2D trajectory with different corners and (b) the 3D shape of the printed part

With detected corners in thermal images, stitching, and localization, the deposited width extraction process in Section 2.3 and 2.4 is performed. Note that only the thermal images with sufficient newly printed corners, whose temperature T_p satisfy $140°C \leqslant T_p \leqslant 150°C$, are further processed for monitoring accuracy. According to the monitored real deposited width, the deposition width error Δw is calculated according to Eqs. (31) and (32). The desired path width w_0 for a straight line in Eq. (31) is related to the feed deposit rate ratio α, and the relationship between them acquired by the experiment is expressed as $w_0 = K_{w\alpha}\alpha + b_w$, where the values of $K_{w\alpha}$ and b_w are experimentally identified [32]. The

identification process included a series of experiments that printed a one-layer straight line part in different α and measured the corresponding change of w_0. The final identified result for $K_{w\alpha}$ and b_w is 3.44 mm and 0.67 mm, respectively. According to the deposition width error Δw, the local deposition inaccuracy rate $\Delta E(t)$ is calculated by Eq. (33). The deposition correction gain K_e is determined by experiment as $K_e = 1 + (150 - T_p)/15$, where T_p is the corner point temperature. For generating input deposition compensation velocity from $\Delta E(t)$, the time constant τ in Eq. (34) of the deposition dynamics for the used printer is identified. The identification process collected the step response of the deposition system of the MEX 3D printer. The identified result for τ is 0.0873 s [32]. The minimum and maximum compensation velocities in Eq. (39) have been set to $\Delta V_{\min} = -2$ mm/s and $\Delta V_{\max} = 4$ mm/s, respectively. The time extension for the dynamic compensation (i.e., the time interval from $\Delta \hat{t}_0$ to Δt_0 and from Δt_1 to $\Delta \hat{t}_1$) is both set at 0.1s. The calculated input compensated deposition velocity $v_{ef}(\Delta t)$ is sent to the printer for compensation.
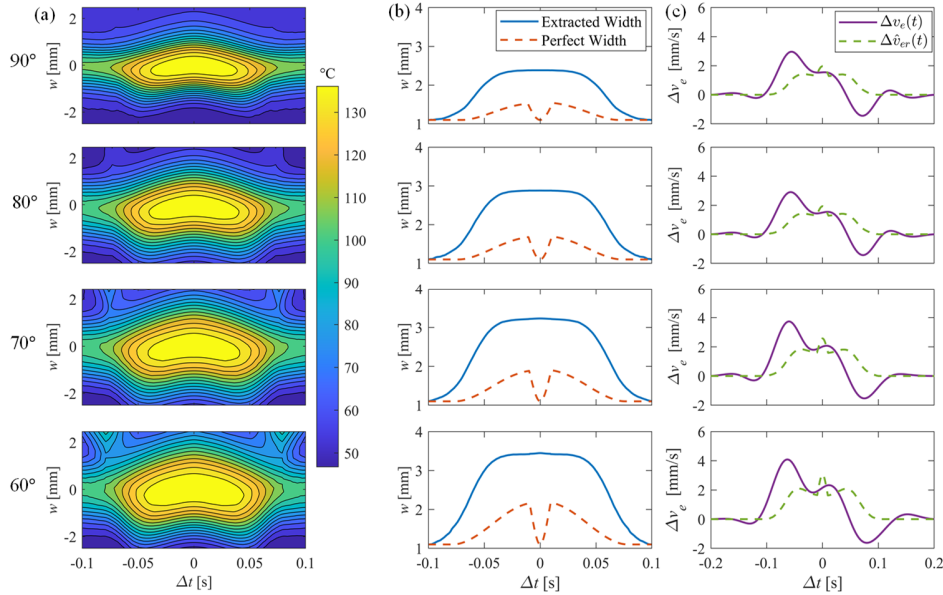

Figure 8 (a) The temperature distribution, (b) extracted and desired width, and (c) deposition compensation sequence for different corners in the printed part

3.3. Printing Results and Evaluation

To evaluate compensation accuracy, the parts with and without the proposed T-DDTC methods are 3D printed. The one-layer verification experiment is first conducted to illustrate the improvement of deposition accuracy in 2D. Figure 8 shows the temperature distribution, extracted and desired width, and the deposition compensation sequence for different corners in the printing part. It is observed that the over-deposition problem is consistently shown across various corners, and the generated compensation sequences are similar. The computation time to generate the compensation sequence by T-DDTC for each corner is about 0.5 s, mainly from AI-based thermal image processing and the corresponding optimal compensation signal generation. The one-layer testing parts include 4 types of corners, so the total time consumption for generating the compensation sequence is about 2 s, while the printing takes about 10 s. As the compensation generation and the printing are executed simultaneously and printing time

18

completely covers the compensation generation time, the total printing time is not affected by employing T-DDTC. Figure 9 illustrates the printing result for different corners without and with compensation from the one-layer verification experiment. As the printed corners are smoothed out due to the deposition dynamics, to enhance the visual effects, Figure 10 highlights the desired- and over-deposition area for the parts shown in Figure 9. It is observed the printing result without compensation suffers over-deposition problems in corners while the result with compensation shrinks the over-deposition region significantly. For evaluating improvement in the over-deposition level for different corners, a 2D over-deposition index at the corner region O_E is introduced. The O_E at the corner region is defined as

$$O_E = \frac{A_o}{A_c},\tag{40}$$

where A_o is the over-deposited area, and A_c is the perfect corner polytope area in a corner. The average over-deposition index for this print has dropped from 106.75% to 31.73%, indicating an enhancement in deposition accuracy.
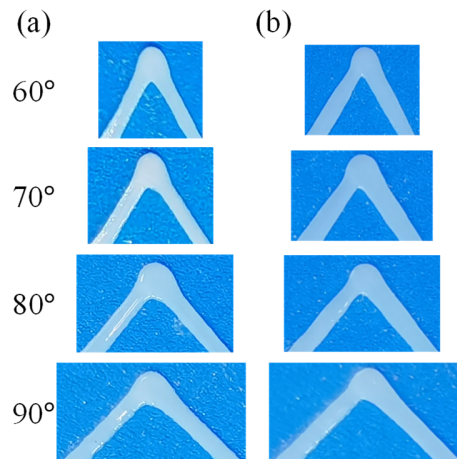

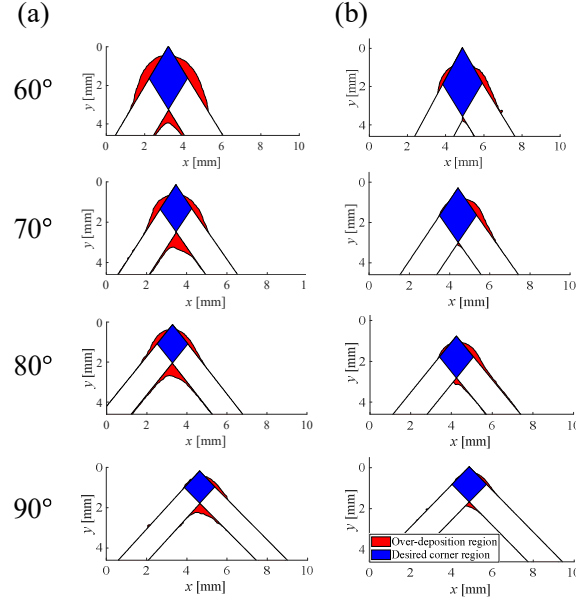Figure 9 The images of one-layer corners without (a) and with (b) proposed compensation

Figure 10 The highlighted one-layer over- and desired-deposition region for corners without (a) and with (b) proposed compensation shown in Figure 9

After one-layer verification, the testing parts with and without compensation were printed, as shown in Figure 11 (a) and (b). The testing parts share the same trajectory as the one-layer experiment. For the multi-layer testing parts, their external surface geometry accuracy is evaluated as the validation of T-DDTC. A Keyence LJ-V7300 2D laser profiler was applied to obtain the printing parts' external surface profiles with a z-axis sampling spacing of 0.5 mm. The measuring system setup is shown in Figure 12. The deposition deviation e_t corresponding to each point $(x_t, y_t) \in \boldsymbol{P}_t$, where $\boldsymbol{P}_t$ is a set of points representing the desirable external surface profile in a specific layer, is obtained after measuring. The coordinate (x_t, y_t) of each point in the set $\boldsymbol{P}_t$ is obtained from the CAD file of the printed part. The deposition deviation e_t with its corresponding (x_t, y_t) composite the element $(x_t, y_t, e_t) \in \boldsymbol{e}_t$, where $\boldsymbol{e}_t$ is the error set. To calculate the error set that shows the difference between the desirable profile and the measured one, another point set $\boldsymbol{P}_m$ consisting of the points (x_m, y_m) representing the measuring profile of the same layer is defined. The deposition contour error e_t at a specific (x_t, y_t) is thus calculated as

$$e_t = \min_{(x_m, y_m) \in \boldsymbol{P}_m} \| (x_t, y_t) - (x_m, y_m) \|. \tag{41}$$

The error set $\boldsymbol{e}_t$ for every layer with the sampled measuring profile was calculated, and the results for all of $\boldsymbol{e}_t$ belonging to the parts with and without compensation (shown in Figure 11 (a) and (b)) are illustrated in Figure 11 (c) and (d), respectively. After the monitoring and compensation system intervened, the maximum deviation is reduced from 1.6805 mm to 0.2468 mm, and the mean value is decreased from 0.4301 mm to 0.2017 mm, as shown in Table 3.

Table 3 The deposition deviation with and without T-DDTC

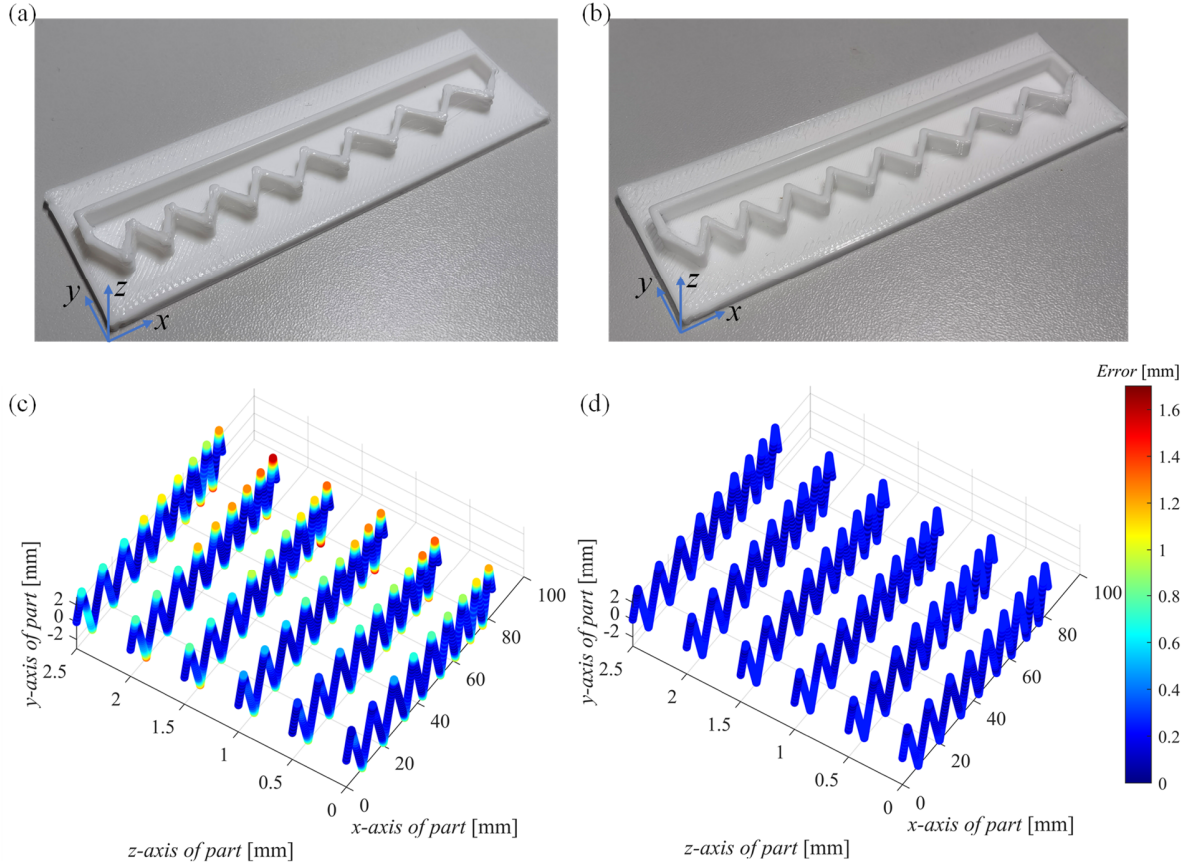|	MAX	RMS
Conventional	1.6805 mm	0.4301 mm
T-DDTC	0.2468 mm	0.2017 mm
Error reduction	85.31%	53.10%

Figure 11 The printed part (a) without and (b) with T-DDTC, along with its deposition contour error measurement (c) without and (d) with T-DDTC
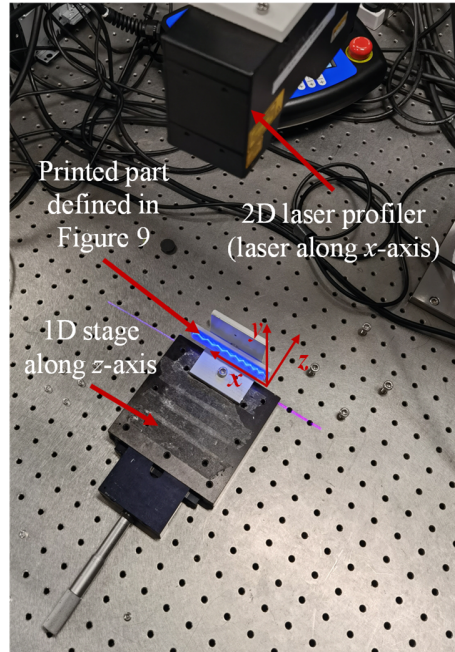
Figure 12 Surface profile measurement setup with 2D laser profiler

4. Conclusions

This paper proposed a thermal-image-enabled dynamic deposition trajectory compensation (T-DDTC) method for material extrusion process. It exploited the in-situ thermal image to extract the deposition trajectory as feedback. An analytical model describing the dynamic relationship between deposition/motion trajectory and the printed path geometry was established. A particular deposition slender condition was established for low-curvature trajectory regions. For the high-curvature trajectory regions, a deposition direction allocation algorithm was established to smoothly define the deposition direction to enable the alignment of the spatial deposition path to the time-domain deposition trajectory. The collected thermal images were sent to the systems to detect the key feature points with fast region-based convolutional neural networks and feature pyramid networks. The feature points help automatically localize the thermal image with the given trajectory. The alignment and the allocated deposition direction synergistically contribute to extracting the deposition inaccuracy at every instant during the process. With the deposition inaccuracy and the identified deposition dynamics, the deposition signal was compensated under a filtered basis framework to alleviate the inaccuracy. The proposed T-DDTC was validated in material extrusion experiments. A representative part was printed with the conventional trajectory and the trajectory with the T-DDTC method. The deposition accuracy enhancement was verified with image-based deposition inaccuracy extraction and 2D laser profiler measurements.

Declaration of Generative AI and AI-assisted technologies in the writing process

The writing process only uses ChatGPT and Grammarly AI to perform grammar checks.

References

[1] K. V. Wong, A. Hernandez, A Review of Additive Manufacturing, ISRN Mechanical Engineering. 2012 (2012) 1–10. https://doi.org/10.5402/2012/208760.

[2] H. Bikas, P. Stavropoulos, G. Chryssolouris, Additive manufacturing methods and modeling approaches: A critical review, International Journal of Advanced Manufacturing Technology. 83 (2016) 389–405. https://doi.org/10.1007/s00170-015-7576-2.

[3] I. Gibson, D. Rosen, B. Stucker, M. Khorasani, Additive Manufacturing Technologies, Springer International Publishing, Cham, 2021. https://doi.org/10.1007/978-3-030-56127-7.

[4] H. Lhachemi, A. Malik, R. Shorten, Augmented Reality, Cyber-Physical Systems, and Feedback Control for Additive Manufacturing: A Review, IEEE Access. 7 (2019) 50119–50135. https://doi.org/10.1109/ACCESS.2019.2907287.

[5] S.K. Everton, M. Hirsch, P.I. Stavroulakis, R.K. Leach, A.T. Clare, Review of in-situ process monitoring and in-situ metrology for metal additive manufacturing, Mater Des. 95 (2016) 431–445. https://doi.org/10.1016/j.matdes.2016.01.099.

[6] T.D. Ngo, A. Kashani, G. Imbalzano, K.T.Q. Nguyen, D. Hui, Additive manufacturing (3D printing): A review of materials, methods, applications and challenges, Compos B Eng. 143 (2018) 172–196. https://doi.org/10.1016/j.compositesb.2018.02.012.

[7] R.B. Kristiawan, F. Imaduddin, D. Ariawan, Ubaidillah, Z. Arifin, A review on the fused deposition modeling (FDM) 3D printing: Filament processing, materials, and printing parameters, Open Engineering. 11 (2021) 639–649. https://doi.org/10.1515/eng-2021-0063.

[8] Y. Fu, A. Downey, L. Yuan, A. Pratt, Y. Balogun, In situ monitoring for fused filament fabrication process: A review, Addit Manuf. 38 (2021). https://doi.org/10.1016/j.addma.2020.101749.

[9] Y. Tlegenov, W.F. Lu, G.S. Hong, A dynamic model for current-based nozzle condition monitoring in fused deposition modelling, Progress in Additive Manufacturing. 4 (2019) 211–223. https://doi.org/10.1007/s40964-019-00089-3.

[10] H. Zhang, X. Zhao, In-situ thermal monitoring informed modeling and simulation of process temperature during vat photopolymerization additive manufacturing, Mater Today Proc. 70 (2022) 237–241. https://doi.org/10.1016/j.matpr.2022.09.027.

[11] M. Khanzadeh, S. Chowdhury, M.A. Tschopp, H.R. Doude, M. Marufuzzaman, L. Bian, In-situ monitoring of melt pool images for porosity prediction in directed energy deposition processes, IISE Trans. 51 (2019) 437–455. https://doi.org/10.1080/24725854.2017.1417656.

[12] M. Khanzadeh, W. Tian, A. Yadollahi, H.R. Doude, M.A. Tschopp, L. Bian, Dual process monitoring of metal-based additive manufacturing using tensor decomposition of thermal image streams, Addit Manuf. 23 (2018) 443–456. https://doi.org/10.1016/j.addma.2018.08.014.

[13] M.H. Farshidianfar, A. Khajepour, A.P. Gerlich, Effect of real-time cooling rate on microstructure in Laser Additive Manufacturing, J Mater Process Technol. 231 (2016) 468–478.

https://doi.org/10.1016/j.jmatprotec.2016.01.017.

[14] G. Ukpai, B. Rubinsky, A three-dimensional model for analysis and control of phase change phenomena during 3D printing of biological tissue, Bioprinting. 18 (2020). https://doi.org/10.1016/j.bprint.2020.e00077.

[15] F. Caltanissetta, G. Dreifus, A.J. Hart, B.M. Colosimo, In-situ monitoring of Material Extrusion processes via thermal videoimaging with application to Big Area Additive Manufacturing (BAAM), Addit Manuf. 58 (2022) 102995. https://doi.org/10.1016/j.addma.2022.102995.

[16] M. Mazzarisi, A. Angelastro, M. Latte, T. Colucci, F. Palano, S.L. Campanelli, Thermal monitoring of laser metal deposition strategies using infrared thermography, J Manuf Process. 85 (2023) 594–611. https://doi.org/10.1016/j.jmapro.2022.11.067.

[17] X. Li, S. Siahpour, J. Lee, Y. Wang, J. Shi, Deep learning-based intelligent process monitoring of directed energy deposition in additive manufacturing with thermal images, Procedia Manuf. 48 (2020) 643–649. https://doi.org/10.1016/j.promfg.2020.05.093.

[18] Z. Li, Z. Zhang, J. Shi, D. Wu, Prediction of surface roughness in extrusion-based additive manufacturing with machine learning, Robot Comput Integr Manuf. 57 (2019) 488–495. https://doi.org/10.1016/j.rcim.2019.01.004.

[19] Q. Tian, S. Guo, E. Melder, L. Bian, W. Guo, Deep learning-based data fusion method for in situ porosity detection in laser-based additive manufacturing, Journal of Manufacturing Science and Engineering, Transactions of the ASME. 143 (2021). https://doi.org/10.1115/1.4048957.

[20] Y. AbouelNour, N. Gupta, In-situ monitoring of sub-surface and internal defects in additive manufacturing: A review, Mater Des. 222 (2022) 111063. https://doi.org/10.1016/J.MATDES.2022.111063.

[21] M. Mani, B. Lane, A. Donmez, S. Feng, S. Moylan, R. Fesperman, Measurement Science Needs for Real-time Control of Additive Manufacturing Powder Bed Fusion Processes, Gaithersburg, MD, 2015. https://doi.org/10.6028/NIST.IR.8036.

[22] F. Wang, F. Ju, K. Rowe, N. Hofmann, Real-time control for large scale additive manufacturing using thermal images, in: IEEE International Conference on Automation Science and Engineering, IEEE, 2019: pp. 36–41. https://doi.org/10.1109/COASE.2019.8843264.

[23] F. Wang, S. Fathizadan, F. Ju, K. Rowe, N. Hofmann, Print Surface Thermal Modeling and Layer Time Control for Large-Scale Additive Manufacturing, IEEE Transactions on Automation Science and Engineering. 18 (2021) 244–254. https://doi.org/10.1109/TASE.2020.3001047.

[24] N. Li, G. Link, J. Jelonnek, Rapid 3D microwave printing of continuous carbon fiber reinforced plastics, CIRP Annals. 69 (2020) 221–224. https://doi.org/10.1016/j.cirp.2020.04.057.

[25] D. Salehi, M. Brandt, Melt pool temperature control using LabVIEW in Nd:YAG laser blown powder cladding process, International Journal of Advanced Manufacturing Technology. 29 (2006) 273–278. https://doi.org/10.1007/s00170-005-2514-3.

[26] M.H. Farshidianfar, A. Khajepour, A. Gerlich, Real-time control of microstructure in laser additive manufacturing, International Journal of Advanced Manufacturing Technology. 82 (2016) 1173–1186. https://doi.org/10.1007/s00170-015-7423-5.

[27] Z. Zhang, A Flexible New Technique for Camera Calibration, 2000. https://doi.org/10.1109/34.888718.

[28] D. DeTone, T. Malisiewicz, A. Rabinovich, Deep Image Homography Estimation, (2016). http://arxiv.org/abs/1606.03798.

[29]   J. Chen, L. hui Zou, J. Zhang, L. hua Dou, The comparison and application of corner detection algorithms, J Multimed. 4 (2009) 435–441. https://doi.org/10.4304/jmm.4.6.435-441.

[30]   S. Ren, K. He, R. Girshick, J. Sun, Faster R-CNN: Towards Real-Time Object Detection with Region Proposal Networks, Adv Neural Inf Process Syst. 28 (2015). http://arxiv.org/abs/1506.01497.

[31]   T.-Y. Lin, P. Dollár, R. Girshick, K. He, B. Hariharan, S. Belongie, Feature Pyramid Networks for Object Detection, Proceedings of the IEEE Conference on Computer Vision and Pattern Recognition. (2017) 2117–2125. http://arxiv.org/abs/1612.03144.

[32]   M. Duan, S. Chen, Y. Yang, Thermal-image-enabled additive manufacturing process monitoring and extrusion trajectory compensation, in: Proceedings of the ASME 2023 Manufacturing Science and Engineering Conference (MSEC), New Brunswick, US, 2023.

[33]   A. Bellini, S. Güçeri, M. Bertoldi, Liquefier dynamics in fused deposition, J Manuf Sci Eng. 126 (2004) 237–246. https://doi.org/10.1115/1.1688377.

[34]   P. Wu, K.S. Ramani, C.E. Okwudire, Accurate linear and nonlinear model-based feedforward deposition control for material extrusion additive manufacturing, Addit Manuf. 48 (2021). https://doi.org/10.1016/j.addma.2021.102389.

[35]   M. Duan, D. Yoon, C.E. Okwudire, A limited-preview filtered B-spline approach to tracking control – With application to vibration-induced error compensation of a 3D printer, Mechatronics. 56 (2018) 287–296. https://doi.org/10.1016/J.MECHATRONICS.2017.09.002.

[36]   B.C. Russell, A. Torralba, K.P. Murphy, W.T. Freeman, LabelMe: A database and web-based tool for image annotation, Int J Comput Vis. 77 (2008) 157–173. https://doi.org/10.1007/s11263-007-0090-8.

[37]   M. Everingham, L. Van Gool, C. Williams, J. Winn, A. Zisserman, The PASCAL Visual Object Classes Challenge 2012 (VOC2012) Results | BibSonomy, (2012). tp://www.pascal-network.org/challenges/VOC/voc2012/workshop/index.html (accessed July 5, 2023).